Materials Advances

ROYAL SOCIETY OF CHEMISTRY

PAPER

View Article Online
View Journal | View Issue

Cite this: *Mater. Adv.*, 2025, **6**, 6843

APTES modified magnetite nanoparticles as a theranostic nanocarrier: a study of loading and sustained release of daunorubicin

Vivekananda Saha,[a] Pohlee Cheah,[b] Ranajit Saha,[c] Yongfeng Zhao *[b] and Goutam Biswas *[a]

In recent decades, iron oxide nanoparticles have been recognized as effective magnetic resonance imaging (MRI) contrast agents and efficient nanocarriers in various drug delivery systems. In this study, APTES-modified iron oxide nanoparticles (APTES@MNPs) were synthesized using a co-precipitation method. This was followed by the implementation of a modified refluxometric method to investigate the loading and sustained release of the chemotherapeutic drug, daunorubicin. Additionally, the T_2 contrasting ability was examined to elucidate the theranostic properties of drug-loaded nanoparticles. The fabricated nanoparticles were characterized using DLS, FTIR, PXRD, FESEM, TEM, XPS, VSM, TGA, and Raman spectroscopy techniques. The nanoparticles exhibited a high T_2 contrast behavior with r_2/r_1 = 16.5. The kinetic study of drug loading showed that the adsorption model followed pseudo-second-order kinetics with a pseudo-second-order rate constant (k_2) of 0.00134 mg g^{-1} min^{-1} at pH ~ 10. The drug release study showed a result of 72% desorption at pH ~ 5.2, whereas at pH ~ 7.4, it was only 12.6%. In addition, adsorption experiments were performed at pH ~ 10. Furthermore, the adsorption of daunorubicin onto the nanoparticles was supported by computational results. Overall, APTES@MNPs acted as a potent and biocompatible sustained-release drug carrier with good diagnostic properties for anticancer theranostic applications.

Received 20th May 2025,
Accepted 4th August 2025

DOI: 10.1039/d5ma00514k

rsc.li/materials-advances

1. Introduction

Nanotechnology has emerged as a field with multidisciplinary applications, extending beyond the industrial and agricultural sectors to exhibit revolutionary potential comparable to that of new medical innovations.[1–8] In recent years, nanotechnology has offered several techniques with promising results, such as the precise diagnosis of complex diseases, gene therapy, targeted therapy, biomarker mapping, and drug delivery through the development of various nanomaterials.[9,10] In anticancer treatment, chemotherapy is known for its potent effectiveness.[11] Various potent chemotherapeutic drugs are used, such as alkylating agents (cisplatin, lomustine), antimetabolites (floxuridine, 5-flurouracil), plant-based alkaloids (paclitaxel, docetaxel, etoposide, and teniposide), and antitumor drugs (doxorubicin, daunorubicin, and valrubicin). In addition to their efficacy, these drugs have several adverse effects, including precise selectivity towards the target, toxicity to both normal and tumor cells, and the issue of multidrug resistance.[12] In cancer treatment, nanotechnology is a new and promising method. It can overcome the major problems associated with traditional treatments, such as radiation, surgery, laser therapy, and chemotherapy. Moreover, the development of a nanostructured drug delivery system capable of transporting therapeutic agents and effectively penetrating tumor cells while avoiding mineralization in the bloodstream is of paramount importance. Thus, a minimum drug concentration is necessary, primarily to prevent its administration to healthy cells.

Over the past two decades, magnetite nanoparticles (MNPs) have been used for theranostic (both therapeutic and diagnostic) cancer treatments. Due to their ultra-small size range (10–100 nm), their distinctive chemical and physical properties are linked to various key factors in the advancement of biomedical approaches.[13] Their exceptional superparamagnetic characteristics and low toxicity enable them to function as MRI contrast agents with excellent imaging capacity.[14] When used as contrast agents in MRI, MNPs demonstrate enhanced magnetization in response to an external magnetic field. Additionally,

[a] *Department of Chemistry, Cooch Behar Panchanan Barma University, Panchanan Nagar, Cooch Behar, WB, 736101, India. E-mail: goutam@cbpbu.ac.in*
[b] *Department of Chemistry, Physics and Atmospheric Science, Jackson State University, P.O. Box 17910, Jackson, MS 39217, USA. E-mail: yongfeng.zhao@jsums.edu*
[c] *Department of Chemistry, National Institute of Technology Manipur, Imphal, Manipur, 795004, India*

they exhibit exceptionally high relaxivity, thereby improving image contrast.[15] MNPs with high surface-to-volume ratios tend to agglomerate, which suppresses their physicochemical activities. Additionally, magnetite nanoparticles with bare surfaces have a high possibility of oxidation and simultaneous loss of superparamagnetism. Functionalization by a potent organic surface coating agent incorporates hydrophilicity with biocompatibility towards nanoparticles.[16]

In the field of drug delivery systems, carbon-based nanoparticles,[17] lysosomes, cell-based carriers, dendrimers,[17] inorganic nanomaterials,[18] micelles,[11] *etc.* have been recognized for their efficacy as nanocarriers, despite some drawbacks.[19] In the widespread area of clinical diagnostics and therapeutic procedures, the development of targeted drug delivery systems has been studied to improve the efficacy of drugs and specificity towards the expected region.[13] Recently, researchers have focused on developing surface-modified MNPs as efficient nano drug carriers.[20] Factors such as easy route of delivery, higher specificity towards cancer cells over normal cells, efficient endocytic capability, low care cost, and high superparamagnetic characteristics place them in advantageous positions over other nanocarriers. Similarly, despite certain nominal disadvantages, surface-modified MNPs function as bioactive carriers in targeted drug delivery to specific sites within the body, facilitated by external magnetic fields.[21] Modification of the surface with high-affinity ligands is suitable for interactions with different cancerous cells, which further develops their selectivity.[22,23] MNPs are also known to modify the pharmacokinetic properties of drugs by decreasing cytotoxicity and increasing the time of sustained release and half-life of drugs. Moreover, surface fabrication can increase the possibility of drug-loaded MNPs in cancerous cells, which further diminishes the lethality rate of normal cells in cancer treatment through chemotherapy.

Daunorubicin is a toxic anthracycline aminoglycoside and a widely used antitumor agent in the chemotherapeutic treatment of acute lymphocytic leukemia.[15,24] Generally, it interacts with DNA and produces reactive oxygen species,[25] which further leads to the apoptosis of cells. In addition to its anticancer properties, it has serious side effects, including oral ulcers, severe heart-related issues, and kidney problems. It is well known that the extracellular pH environment of tumor cells is slightly acidic (4.5 to 6.2), whereas the pH of blood is 7.4.[26,27] According to Cancer Research UK (CRUK), chemotherapeutic treatment using daunorubicin as a drug requires 12 cycles, each lasting 21 days. Daunorubicin has a half-life of 18.5 h after administration in the human body, 25 percent of which is metabolized in the liver and 75 percent excretion is excreted through biliary action.[28] If the excretion time from the body is delayed by some action, it will be beneficial for therapeutic treatment. Therefore, the drug needs to remain in the body for a longer time for effective and sustained release of daunorubicin at the cancer cells. Recently, various advanced techniques have been developed for selective drug carriers in the therapeutic world of medicinal chemistry. The sustained and targeted liberation of chemotherapeutic drugs is associated with multiple disagreements. Various factors, including different temperatures, pH, and selective enzymes, have been used to tackle the challenges of distinguishing healthy and cancerous cells. Hence, to be an efficient drug delivery agent, it should have the capacity to retain the drug in the bloodstream and potent releasing properties at lower pH inside cancerous cells.[29] Thus, surface-modified MNPs have been identified as a potential solution to these challenges.[30] In this context, the adsorption kinetics of daunorubicin on 3-aminopropyltriethoxysilane (APTES)-modified MNPs (APTES@MNPs) were assessed across various pH levels, and the drug's controlled release over time was examined. The adsorption mechanism was theoretically validated. Computational prediction was performed to estimate the values of molecular energy levels regarding the loading of daunorubicin on APTES@MNPs. The difference in the HOMO–LUMO energies provides additional support for loading the drug onto the fabricated nanoparticles. Additionally, T_2 and T_1 relaxation studies were performed to present a clear picture of the MRI contrast capability.[31]

2. Materials and methods

2.1 Materials and chemicals

APTES, iron(III) chloride hexahydrate ($FeCl_3{\cdot}6H_2O$), iron(II) chloride anhydrous ($FeCl_2$ anhydrous), sodium hydroxide (NaOH) pellets, sodium phosphate monobasic dihydrate (NaH_2PO_4), sodium phosphate dibasic dihydrate ($NaHPO_4$), and daunorubicin hydrochloride were of analytical grade. A centrifuge machine (Remi R-8C), ultrasonicator (Qsonica Sonicator), pH meter (Fisher Scientific Accumet (Model AB 250)), UV-Visible (UV-VIS) spectrophotometer (Thermo Evolution 201), dynamic light scattering (DLS, Litesizer 500, Anton Paar), FT-IR spectrophotometer (PerkinElmer), and Niumag relaxometer (0.5 T) were typical instruments used for conducting investigations.

2.2 Synthesis of APTES modified iron oxide nanoparticles (APTES@MNPs)

First, superparamagnetic iron oxide nanoparticles were synthesized using an efficient co-precipitation method at room temperature.[32] Subsequently, the solid precipitate was vacuum-dried at 70 °C for 12 h to obtain bare iron oxide.[23,33–36]

Previously, APTES modification has been proposed using different methodologies, including the use of an inert atmosphere, organic solvents such as toluene, and large stoichiometric amounts of APTES, which may be expensive for industrial production. In this study, surface modification was conducted using a cost-effective approach.[37,38] Subsequently, minor adjustments were implemented to further enhance the surface modification. 1.0 g of MNPs was placed in a 250 mL round-bottom flask with 100 mL of 80% methanol in water and basified using a measured amount of NaOH solution to pH ~ 10, followed by ultrasonication to obtain a suspension. Next, 1.8 mL of APTES was added, and the mixture was refluxed

at 60 °C for 20 h. The nanoparticles were separated using a permanent magnet, washed with methanol three times, and vacuum-dried at 50 °C for 24 h.[34,37,38]

2.3 Characterization

2.3.1. Dynamic light scattering (DLS) and zeta potential study. Dynamic light scattering (DLS) was performed to validate the synthesized nanoparticles. The Smoluchowski equation was used to perform the operation under a detector angle of 633 nm wavelength light at 25 °C, and a very dilute well-dispersed solution of nanoparticles was taken.[39] Using this technique, the zeta potential and hydrodynamic size of the nanoparticles were measured before and after drug loading and desorption.

2.3.2. Fourier transform infrared (FTIR) spectrum analysis. Fourier-transform infrared (FTIR) spectroscopy was performed to investigate the functionalization of the free nanoparticles, APTES@MNPs and DA@APTES@MNPs. Both attenuated total reflection (ATR) and KBr pellets were used to analyze two batches of samples in the FT-IR analysis (32 scans of each) between 400–4000 cm^{-1}.

2.3.3. Powdered X-ray diffractometry (PXRD) analysis. PXRD was performed to obtain a clear observation of the crystalline structure of the compounds and phase purity, and to identify their active ingredients. A Rigaku MiniFlex 600 X-ray diffractometer (40 kV, 15 mA) using Cu Kβ radiation (λ = 0.154 nm) was used to conduct the PXRD analysis of APTES@MNPs. The scan degree ranged from 10° to 80°, with a step degree of 0.01 at a rate of 1° min^{-1}.

2.3.4. Field emission scanning electron microscopy (FESEM) and energy dispersive X-ray spectroscopy (EDS-MAP) analysis. Field emission scanning electron microscopy (FESEM) was used to examine the exact shape and structure of the surface, especially the structural integrity of the fabricated nanoparticles. Moreover, EDS analysis revealed the chemical composition of the synthesized nanoparticles.[40]

2.3.5. Transmission electron microscopy (TEM) analysis. TEM accelerates electrons through samples and collects the transmitted electrons to image materials at the nanoscale level. This analysis is important for estimating the actual size of nanoparticles. Transmission electron microscopy (TEM, JEOL JEM 1011) was used for this analysis. An ultrathin 150-mesh carbon-coated grid was coated with the produced nanoparticles, dried, and examined.[34]

2.3.6. Vibrating sample magnetometry (VSM) analysis. The magnetic properties of the APTES@MNPs were measured using vibrating sample magnetometry by taking 15 mg of the sample at a 2 T magnetic field.[41]

2.3.7. Thermogravimetric analysis (TGA). TGA analysis provides information about nanoparticle stability and coating of the nanoparticles.[42,43] TGA was performed on a Shimadzu DTG-60 instrument from room temperature to 600 °C using an aluminum (Al) crucible under a nitrogen gas flow of 10 mL min^{-1}.

2.3.8. Raman spectroscopic measurement. Raman analyses were carried out in an air cooled charge coupled device detector of a LabRAM HR 800 Horiba JY LabRam HR Evolution Spectrometer, with a 633 nm laser using a power of <1 mW (objective lens: 50×) and a diffraction grating of 1800 grooves per mm. The spectrum was obtained at room temperature using backscattering geometry.

2.3.9. X-Ray photoelectron spectroscopy (XPS) measurements. XPS measurements were performed using an ESCA spectrometer (SPECS Surface Nano Analysis GmbH, Germany) associated with Al K-alpha (1486.61 eV) X-rays of 13 kV and 100 W at room temperature.

2.4. Drug loading and release experiment

Recently, nanocarriers have emerged as reliable alternatives not only for therapeutic treatment but also for the diagnosis of several diseases.[44,45] In modern cancer treatment, chemotherapeutic drug-loaded nano systems are used in a well-established and effective manner. Hence, the study of the kinetic path of drug loading and their sustained, more precise, and long-term controlled release has gained remarkable importance for theranostic applications. The adsorption of the chemotherapeutic drug daunorubicin onto APTES@MNPs was investigated at room temperature using phosphate buffer as the solvent. A fixed amount of daunorubicin was added to prepare the adsorbate solution for the adsorption study at different pH values (3–10) against a specific amount of nano sorbent. These conditions were applied to achieve the best pH, where the nanoparticles exhibited the highest efficacy. In this study, to perform all the adsorption experiments, the concentration of daunorubicin was set at 20 mg L^{-1} in 10 mL of solution against a constant amount of 10 mg of nano sorbent. The solutions were treated in a mechanical shaker for 360 min to achieve adsorption saturation. After the experiment, the nano sorbents were removed using a permanent magnet, and aliquots were taken from the solution for analysis using a UV-VIS spectrophotometer at λ_{max} 282 nm for daunorubicin. The percentage of drug loading and equilibrium adsorption capacity were calculated using eqn (1) and (2),[46] respectively.

$$\%\ \text{drug loading} = \frac{(C_0 - C_t)}{C_0} \times 100 \quad (1)$$

And the equilibrium adsorption capacity (mg g^{-1}),

$$Q_e = \frac{(C_0 - C_e)}{m} \times V \quad (2)$$

C_0, C_t, and C_e are the initial, at time t, and equilibrium concentrations of the drug in mg L^{-1}, respectively. The mass of the nano sorbent and the volume of the solution are denoted by m (mg) and V (mL), respectively.

The release behavior of daunorubicin from DA@APTES@MNPs was measured three times to ensure repeatability. For the desorption analysis, 50 mg of daunorubicin-loaded APTES@MNPs was placed in 2 mL of phosphate buffer (pH 5.2 and 7.4) and shaken in a perpendicular mechanical shaker at 298 K. A 100 μL aliquot was removed from both pH systems, and the supernatant was removed from the nanoparticles using a permanent magnet (Fig. S1). Desorption was observed using a UV-VIS spectrophotometer at predetermined

points for up to 100 h, and the % drug release was calculated. After each interval, an equal amount of fresh pH solvent was added to the mixture. Liquid chromatography–mass spectrometry (LCMS) data of the solution after the desorption study were also investigated to confirm the presence of daunorubicin within the solution.

2.5. Computational study

The Fe_3O_4 inverse spinel structure contains two Fe^{3+} cations, one Fe^{2+} cation, and four O^{2-} anions. In the model, another Fe^{3+} was added to form $Fe_4O_4{}^{3+}$, a cubic moiety (FO), where the metal ions and O^{2-} ions occupy alternate positions on the cube.[47–49] One APTES ligand was connected to one of the Fe centers through Fe–O–Si linkages, rendering the entire complex neutral. The resulting compound was denoted as FO-A. The drug daunorubicin might create bonds *via* a condensation reaction mechanism and finally form a complex (C). Furthermore, the geometries of FO, FO-A, and C were optimized at the RI-BP86-D3(BJ)/def2-SVP level of theory. Both doublet and dectet spin multiplicities were considered for computations. Calculations were performed using the ORCA 5.0.4 program package.

2.6. MRI relaxivity study

MNPs are known for their unique superparamagnetic properties, which incorporate magnetic field inhomogeneities.[50,51] In MRI diagnosis systems, to obtain high-contrast images of the affected areas in the human body, MNPs have been used as T_2 contrast agents.[52] The choice of MNPs over a potent T_1 contrast agent, such as gadolinium (Gd), was mainly due to the adverse effects of Gd deposition inside the body. Additionally, the efficacy of MNPs is enhanced because of their low toxicity and biocompatibility, allowing them to be easily excreted from the body after diagnosis. Additionally, the chemical environment around the nanoparticles and their surface properties can manipulate the relaxation times of water molecules.[53] To investigate the magnetic relaxation properties of APTES@MNPs, the longitudinal (T_1) and transverse (T_2) relaxation times of the dispersion of grafted nanoparticles at increasing iron concentrations were measured using a Niumag 0.5 T relaxometer at 32 °C with the following parameters: SF, 18 MHz; TW, 5000 ms; SW, 100 kHz; RG, 20 dB; DRG1,3. NMR Analysis Software Ver. 4.0 was used to compute for both T_1 and T_2. Furthermore, MRI-T_2 weighted phantom images were acquired using a spin-echo (SE) sequence: TR/TE = 5000/150 ms.

3. Results and discussion

3.1. Characterizations

3.1.1 DLS and zeta potential analysis. DLS analysis was performed to determine the hydrodynamic size of the fabricated nanoparticles before and after adsorption. The findings demonstrated that the APTES@MNPs exhibited monodispersity, as evidenced by a polydispersity index (PDI) value of 0.23 and a hydrodynamic size of 670.1 nm.[54] After the drug was adsorbed onto the nanoparticles, the theoretical size was expected to be larger, which was further validated by the practical outcomes with a hydrodynamic size of 1365.3 nm (PDI = 0.25) (Fig. 1a). The zeta potential of APTES@MNPs at different pH values was studied to calculate the point of zero charge (PZC) (Fig. 1c) and the PZC value was 9.6. As a result, below pH ~ 9.6, the surface charge was positive and negative at pH values greater than 9.6. The hydrodynamic size after drug release from the nanoparticles was 858.2 nm (PDI = 0.1), indicating that the nanoparticles retained their original size before the adsorption experiment. Furthermore, the zeta potentials of the non-loaded, loaded, and released nanoparticles at neutral pH were +32.2, −25.1, and −0.8 mV, respectively (Fig. 1b). Such a high positive charge for the bare nanoparticles was due to the surface coating by the $-NH_3{}^+$ group of the APTES moieties, and the negative value of the zeta potential after the adsorption experiment represents the adsorption of the drug onto the nanoparticles. For the desorbed nanoparticles, the zeta potential increased, confirming the desorption of daunorubicin from the nanoparticles.

3.1.2. FTIR analysis. FTIR spectroscopy verified the presence of the APTES moiety on the surface of the MNPs and provided evidence for the adsorption and desorption of daunorubicin on the nanoparticles. The FTIR spectra of the APTES@MNPs show absorption bands for the silanol (Si–O–H) and siloxane (Si–O–Si) groups at 1045–1109 cm^{-1}.[55] More precisely, Si–O stretching, Si–C stretching, and Si–O–H bending vibrations were observed at 1006, 798, and 892.06 cm^{-1}, respectively.[29] The absorption bands at 1333, and 2920–2850, cm^{-1} were ascribed to C–N and $-CH_2$ asymmetric vibrations, respectively (Fig. 1d).[29,55] The broad band at 1637 cm^{-1} was due to the N–H bending vibration and that at 1320 cm^{-1} corresponds to C–H bending.[29] The characteristic peak for the Fe–O bond at 562 cm^{-1} and broad peaks at 3100–3600 cm^{-1} shows the presence of O–H and N–H bonds.[35,56–58] Additionally, the adsorption of daunorubicin onto the nanoparticles was confirmed using FTIR spectroscopy (Fig. 1d), where a broad peak near 1500–1800 cm^{-1} was observed for the carbonyl and imine stretching frequencies, and the broad peak at 3200 cm^{-1} was attributed to O–H and N–H stretching vibrations. The peak near 1660 cm^{-1} corresponds to the C=N stretching vibration, and the peak near 1618 cm^{-1} indicates the characteristic peak for hydrogen-bonded carbonyl groups of the quinone moiety of daunorubicin (Fig. 1d).

3.1.3. PXRD analysis. The PXRD pattern of APTES@MNPs (Fig. 1e) exhibited diffraction peaks at 2θ = 30.2°, 35.9°, 43.5°, 53.9°, 57.41°, and 63.08° without any characteristic peaks for either hematite or maghemite. In comparison to standard data for magnetite crystals, the peaks correspond to the (220), (311), (400), (422), (511), and (440) crystal planes (ICDD file, no. 00-001-1111) confirming the inverse cubic spinel structure of magnetite (Fe_3O_4).[34,59]

3.1.4. Thermogravimetric analysis (TGA). Thermogravimetric analysis (TGA) (Fig. 1f) is an advanced technique for examining nanoparticle surface properties. The experiment was

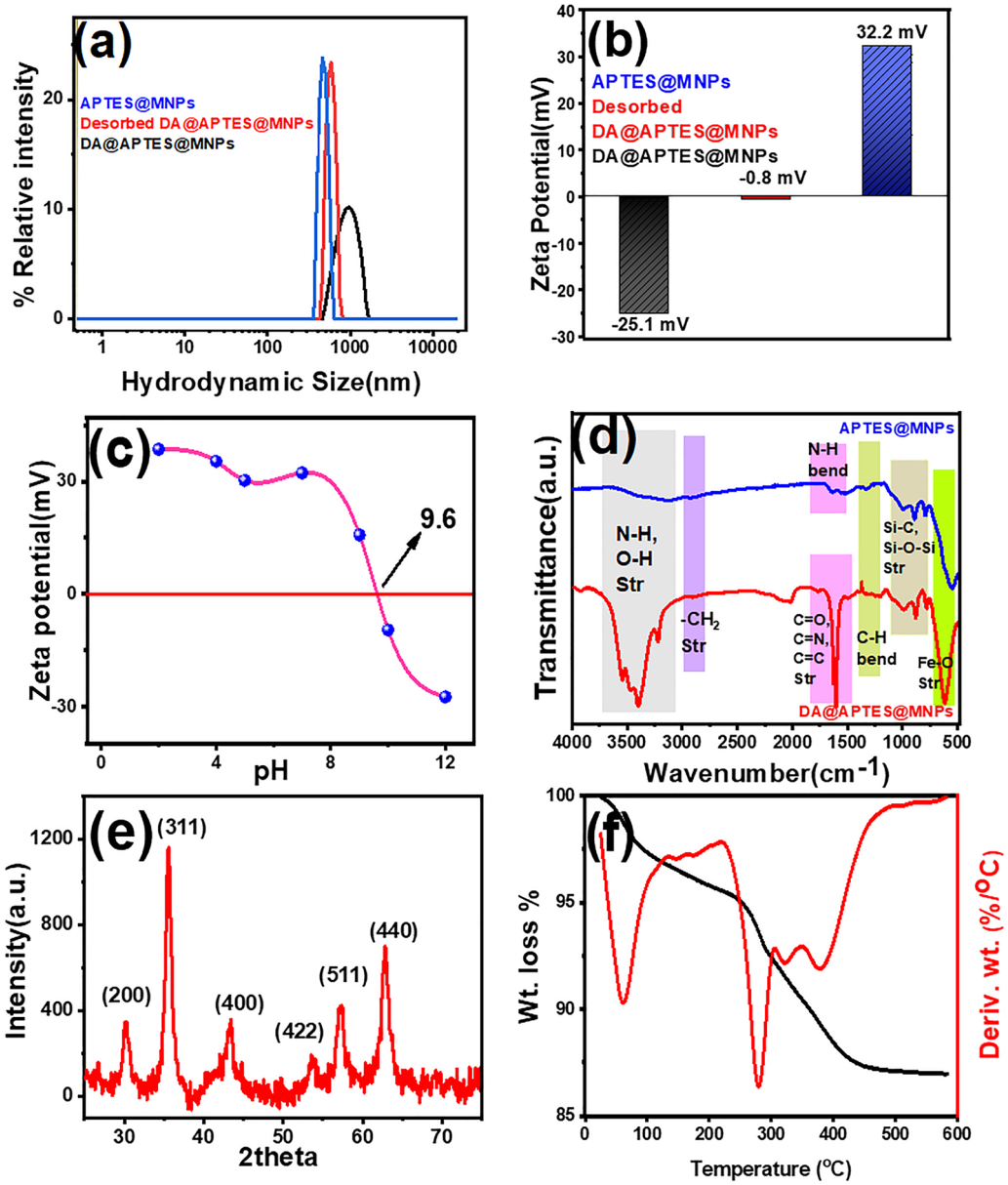

Fig. 1 (a) DLS curve of bare, loaded, and unloaded nanoparticles; (b) zeta potentials of bare, loaded with daunorubicin (DA), and nanoparticle after desorption; (c) PZC plot; (d) FTIR spectral curve; (e) PXRD curve; and (f) TGA curve of APTES@MNPs.

performed in the temperature range of 30–600 °C. The first-step weight loss at approximately 100 °C was observed for the vaporization of water and –OH moieties that were adsorbed on the nanoparticles. The second-step weight loss at 290 °C was much larger than the previous one, indicating the structural change in the magnetite moiety as well as the decomposition of the organic moiety, that is, APTES molecules on the nanoparticles.[60]

3.1.5. FESEM and EDS-MAP analysis. FESEM images of the fabricated nanoparticles (Fig. 2a) were mostly spherical in shape and size. EDS spectra (Fig. 2b–e) show the presence of iron (Fe), silicon (Si), nitrogen (N), and oxygen (O) atoms in the synthesized nanoparticles.[23] The surface coverage of the iron oxide nanoparticles with APTES was confirmed using EDS mapping of the nitrogen and silicon atoms.

3.1.6. TEM analysis. TEM was used to examine the shapes and sizes of the nanoparticles. In Fig. 2f, it can be seen that spherical nanoparticles with minor imperfections, such as slight aggregation, which may be due to the multi-layering of particles on the TEM grid,[42] and a slightly wide size distribution are visible in the TEM images.[61] The magnified TEM image indicates the presence of an APTES layer around the intense region of the Fe_3O_4 moieties (Fig. S2). A histogram was plotted (Fig. 2g), from which we obtained the average size of the APTES@MNPs to be 21.29 nm.

3.1.7. VSM analysis. In the magnetization experiment (Fig. 2h), the coercivity, saturation magnetization (M_s), and retentivity (M_r) were obtained as zero, 67 emu g^{-1}, and 25 emu g^{-1}, respectively. Hence, nanoparticles with zero

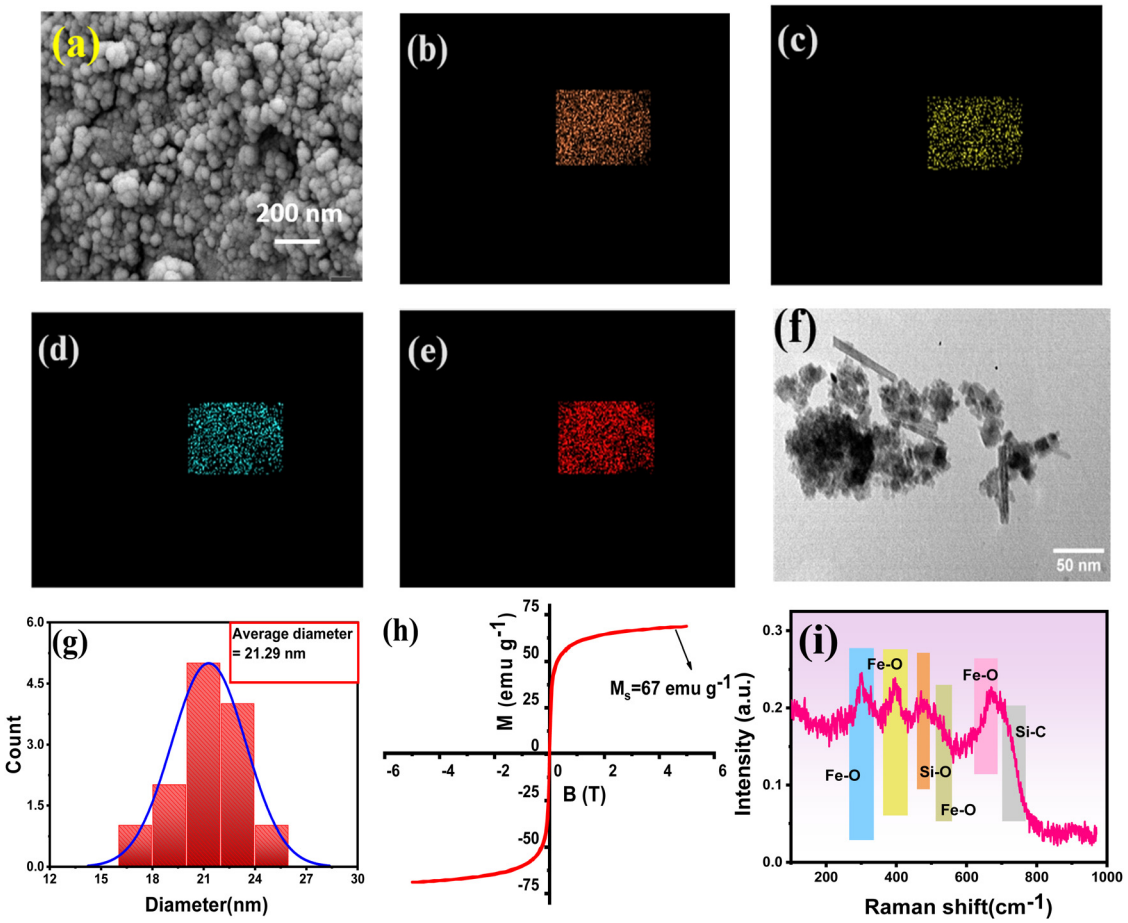

Fig. 2 Characterization plots for APTES@MNPs: (a) FESEM image; (b)–(e) EDS mapping of Fe, Si, N, and O, respectively; (f) TEM image; (g) histogram of TEM; (h) magnetization saturation graph; and (i) Raman spectra of APTES@MNPs.

coercivity and very low remnant magnetism (M_r) in the hysteresis loop exhibit superparamagnetism.[62,63] Compared to bare magnetite nanoparticles (76.4 emu g^{-1}), the APTES@MNPs exhibited a nominal decrement in magnetization, owing to the monolayer coverage of the APTES moiety.[64,65]

3.1.8. Raman spectral analysis. Raman spectra help to establish the exact spinal structure of iron oxide nanoparticles between magnetite, hematite, and maghemite. In Fig. 2i, an intense peak characteristic of magnetite (Fe_3O_4) was observed at 668 cm^{-1} due to A_{1g} vibrations.[66,67] A minor shoulder peak was observed at 703 cm^{-1}, indicating Si–C vibrations of the APTES moiety over the magnetite nanoparticles. The additional peaks at 306 and 396, and the less intense broad peak at 538 cm^{-1} are in good agreement with the Fe_3O_4-type of structure.[66,68] In addition, a peak at 473 cm^{-1} supports the presence of Si–O bonds in the fabricated nanoparticles.[69]

3.1.9. XPS analysis. XPS analysis was performed to observe the electronic state of the surface and the chemical composition of the APTES@MNPs. All the atoms associated with the nano-sorbent were found in the XPS Spectral curve for the entire energy range (Fig. S4). The high-resolution spectrum (Fig. 3a) extracted for the electronic nature of iron atoms present in the Fe_3O_4 moiety. The first two Fe $2p^{3/2}$ peaks with binding energies of 708.3 and 715.9 eV correspond to the Fe^{2+} and Fe^{3+} ions of magnetite.[70]

Additionally, the characteristic peak near 718.2 eV suggests the presence of Fe^{2+} ions, and the remaining three peaks at 724.3, 730.3, and 736.5 eV originated from the Fe $2p^{1/2}$ component of spin–orbit doublets.[71,72] For Si 2p, a characteristic peak for the Si–C bond was observed at 99.3 eV, whereas the other two peaks with binding energies of 104.3 and 107.4 eV were assigned to Si–O bonds in the APTES fabrication around the magnetite moiety (Fig. 3b). The highest peak at 402.3 eV (Fig. 3c) was attributed to NH_3^+ ions, along with another peak with a binding energy of 400.3 eV, which supports the presence of NH_2 moieties. The C 1s spectrum exhibited three peaks at 290.3, 290.6, and 292.2 eV, corresponding to the Si–CH_2, –CH_2–CH_2, and CH_2–NH_2 bonds in the APTES moiety (Fig. 3d).[73] The deconvoluted peaks for O 1s consisted of the characteristic peak of magnetite O^{2-} ions at 532.3 eV and two other peaks at higher binding energy regions designated the oxygen atoms of silanes (Fig. 3e).[74]

3.2. Drug loading and release study with APTES@MNPs

3.2.1. Effect of pH in drug loading. The adsorption of the drug onto the adsorbent depends on the surface charge of both

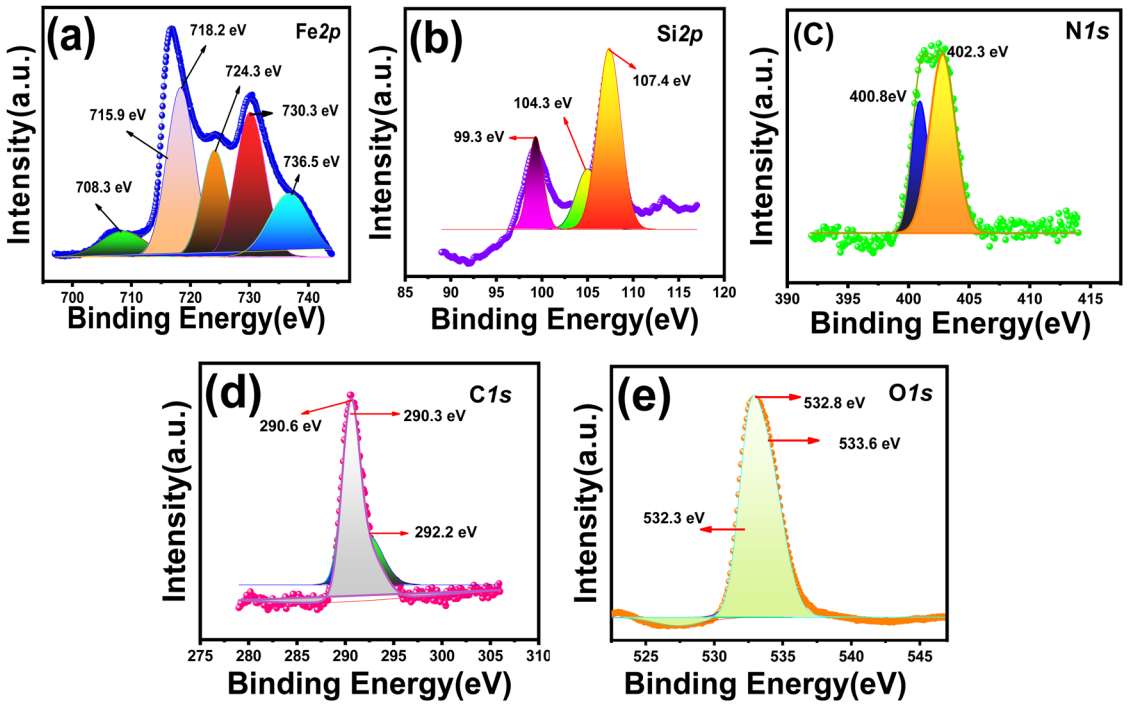

Fig. 3 XPS survey spectral curves of APTES@MNPs. The regions (a)–(e) for the Fe(2p), Si(2p), N(1s), C(1s), and O(1s) peaks, respectively.

systems. Generally, pH has a significant effect on the overall surface charge of a substance, which is governed by the isoelectric point of the respective substances. The pH below the PZC surface charge is positive, and above it, it is negative. Daunorubicin loading was performed through adsorption experiments in different phosphate buffer solutions (PBS) with pH (3–10) by adding 20 mg L^{-1} of drug against 10 mg of APTES@MNPs in 10 mL of each solution (Fig. 4a). At pH ~ 3, 9.63% adsorption of daunorubicin was observed, and a gradual increase in pH was observed, with the highest adsorption of 81.53% at pH ~ 10. As the PZC of the nanoparticles was found at pH ~ 9.6, at lower pH, the surface of the nanoparticles was positively charged, and the daunorubicin with a positively charged surface resulted in a repulsion between the nanoparticle and daunorubicin. At pH ~ 10, the nanoparticles with a nominally negatively charged surface exhibited a high affinity for daunorubicin, which could be the result of chemical interactions, including the formation of imine bonds between the amine groups of the nanoparticles and the carbonyl groups of daunorubicin.

3.2.2. Kinetics study of drug loading. The kinetics of the drug-loading study were analyzed to determine the equilibrium adsorption capacity of the fabricated nanoparticles. Kinetic data were plotted for pseudo-first-order, pseudo-second-order, and interparticle diffusion kinetics determination using eqn (3)–(5), respectively.

$$\ln(Q_e - Q_t) = \ln Q_e - k_1 t \quad (3)$$

$$\frac{t}{Q} = \frac{t}{Q_0} + \frac{1}{k_2 Q_e^2} \quad (4)$$

$$Q_t = k_{diff} t^{0.5} + C \quad (5)$$

where Q_0, Q_t, and Q_e are the adsorption capacities at the initial time, time t, and equilibrium time, respectively; k_1 and k_2 are

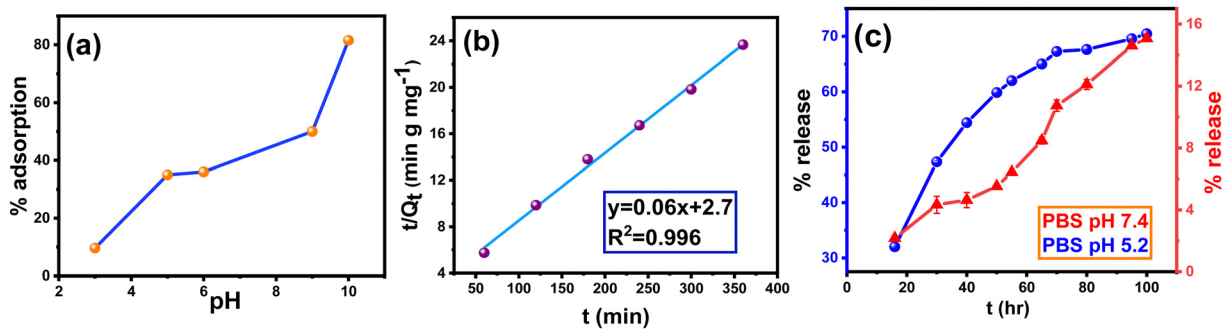

Fig. 4 (a) Curve for the percentage of daunorubicin adsorption at different pH values, (b) pseudo 2nd order kinetics graph for the adsorption of daunorubicin on APTES@MNPs, and (c) release profile of daunorubicin at pH 5.2 and 7.4.

the pseudo 1st and 2nd order rate constants, respectively; and k_{diff} represents the diffusion rate constant.

Furthermore, the adsorption rate constants and kinetic paths of sorption were investigated. The adsorption of daunorubicin followed a pseudo-second-order kinetic path, which was confirmed by a regression constant (R^2) of 0.996 (Fig. 4b), which is closer to pseudo-second-order kinetics than pseudo-first-order kinetics (R^2 = 0.849) (Fig. S3). Based on the literature, the adsorption of daunorubicin on the nanoparticles follows the chemisorption pathway, as some chemical interactions are formed between the sorbate and sorbent surface.[34,75] The pseudo-second-order rate constant (k_2) and equilibrium adsorption capacity (Q_e) were 0.00134 mg g^{-1} min^{-1} and 16.6 mg g^{-1}, respectively. Furthermore, the experimentally observed value of Q_e (15.3 mg g^{-1}) was comparable to the theoretical value. Additionally, by taking 50 mg of nanoparticles against 100 mg L^{-1} of daunorubicin, almost 99% adsorption was achieved at pH ~ 10.

3.2.3. pH monitored sustained drug release study. The desorption or release of daunorubicin from the loaded nanosorbent was studied in PBS at pH ~ 7.4 and 5.2. At pH ~ 5.2, controlled drug release was observed throughout the 100 h experimental period, leading to a remarkable average release of 70.43% (Fig. 4c). In contrast, at pH ~ 7.4, it was mostly retained on the sorbent over time, with a nominal average release of ~15.06% (Fig. 4c) observed after 100 h of reaction. Such a difference between the desorption studies (pH 5.2 and 7.4) might be due to the electrochemical structures of both the nanoparticles and sorbate. Moreover, daunorubicin release was confirmed by LC–MS using an M + H peak at 528.25 (Fig. S5). Consequently, at lower pH values, due to the instability of imine bonds between the carbonyl groups of daunorubicin and the amine groups of nanoparticles, a greater release of drugs was observed. In an acidic environment, the surface of the nanoparticles became positively charged, which might have also created a repulsive interaction with daunorubicin. Prolonged retention of the drug at pH ~ 7.4 indicates the specificity of the delivery system at the desired acidic site (surrounding or inside the tumor cells) without dissolving in the bloodstream. This can suppress the toxic effects of daunorubicin on normal healthy cells.

3.2.4. Computational analysis. The optimized geometries of FO, FO-A, and C with both doublet and dectet spin multiplicities are presented in Fig. 5. In the computational study, the energies of both spin multiplicities were compared. The energy differences illustrate that in the case of the bare complex, FO, the dectet spin multiplicity was slightly more stable by 0.7 kcal mol^{-1} compared to the doublet spin multiplicity. Upon binding with APTES and APTES-daunorubicin, *i.e.* complexes FO-A and C, the doublet geometry was the more stable by 1.8 kcal mol^{-1} and 6.9 kcal mol^{-1}, respectively, compared to their dectet analogues. Moreover, no remarkable changes were observed in the geometries of the electronic states of the studied complexes. The frontier molecular orbitals of C with α spins are shown in Fig. S6. The HOMO was situated on the anthraquinone fragment of daunorubicin. In contrast, the LUMO was based on an iron-oxide cluster.

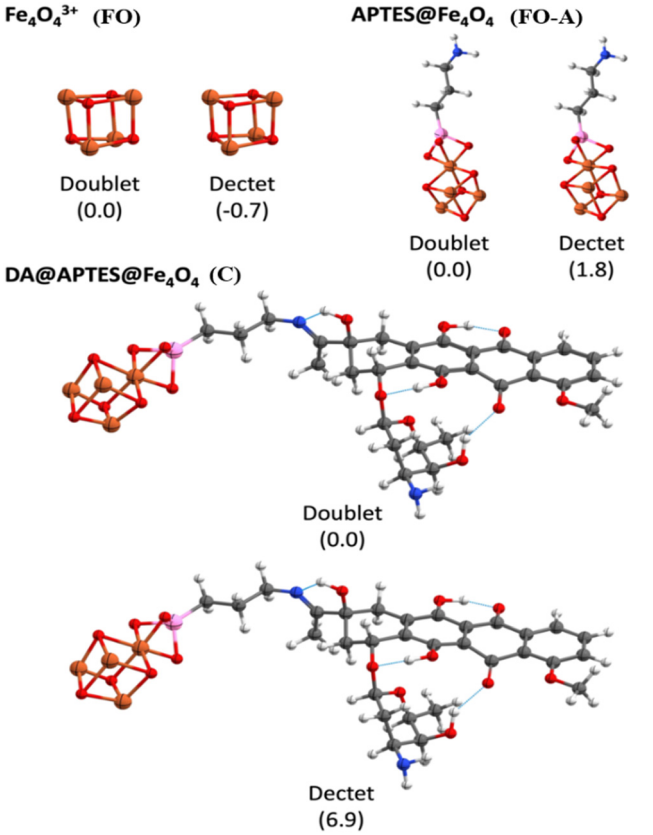

Fig. 5 Optimized geometries of FO, FO-A, and C in both doublet and dectet spin multiplicities at the RI-BP86-D3(BJ)/def2-SVP level of theory. The color codes of the atoms are as follows: H – white; C – grey; O – red; N – blue; Si – pink; Fe – orange.

3.3. Diagnostics study

3.3.1. T_1 and T_2 relaxation analysis. Superparamagnetic iron oxide nanoparticles are well known for their strong

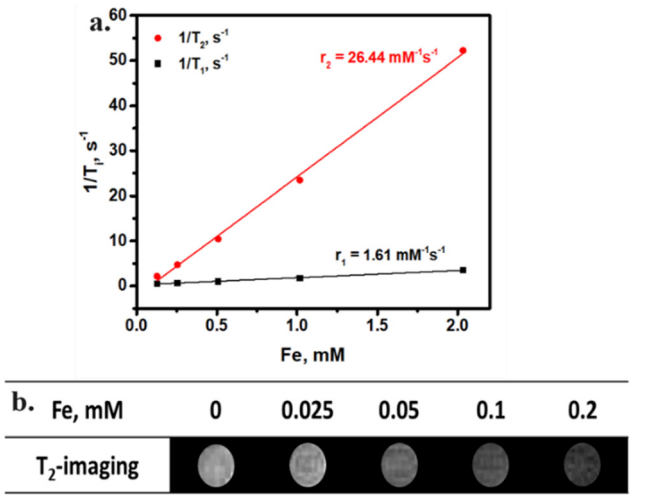

Fig. 6 Magnetic resonance imaging relaxivities and phantom studies. (a) Inverse transverse time (1/T_2) and longitudinal time (1/T_1) *versus* iron concentration and (b) T_2-weighted phantom images.

Table 1 r_1 and r_2 values at different magnetic fields of some reported iron-based nanoparticles

Nanomaterial	r_1 (mM^{-1} s^{-1})	r_2 (mM^{-1} s^{-1})	Magnetic field [$B^0(T)$]
Silica coated Fe_3O_4	1.2	7.8	3[77]
Fe_3O_4	13.31	40.9	1.4[78]
Fe_3O_4–PEG1100	7.3	17.5	1.4[79]
Zinc ferrite	7.93	14.64	1.5[80]
Nickel ferrite	6.85	12.92	1.5[80]
Ultrasmall sized Fe_3O_4	6.15	28.62	1.4[50]
Iron oxide polymag™ clusters	20.5	454	0.68[81]
PAA@Fe_3O_4	8.2	16.7	1.4[82]
APTES@MNPs	1.61	26.44	0.5(This study)

T_2-relaxation effect owing to their intrinsic high saturation magnetization.[51,76] The magnetic relaxivities of APTES@MNPs were studied using a dispersion of nanoparticles in water by plotting the rate of transverse time ($1/T_2$) and the rate of longitudinal time ($1/T_1$) against the iron concentration and computing the corresponding linear slopes to obtain r_2 = 26.44 mM^{-1} s^{-1} and r_1 = 1.61 mM^{-1} s^{-1} (Fig. 6a). This observed value of r_2/r_1 ratio ~16.5 confirmed that APTES@MNPs behaved as a potent T_2-contrasting agent. Eventually, the comparison with the r_2/r_1 ratio values of reported iron oxide-based nanoparticles exerts that the APTES@MNPs have better T_2 contrasting capability in some cases (Table 1). This was further demonstrated by the MRI phantom performance, as shown in Fig. 6b, where the phantom contrast gradually darkened with an increase in the iron concentration to 0.2 mM.

4. Conclusion

In this study, APTES@MNPs were synthesized *via* a modified refluxometric method after preparing bare MNPs using a co-precipitation technique. The synthesis of the nanoparticles was primarily confirmed using DLS measurements. Subsequently, FTIR and Raman analyses were performed to confirm the magnetite structure and functionalization with APTES. Furthermore, the inverse-spinel crystal structure and spherical shape of the nanoparticles were determined using PXRD and FESEM analyses, respectively. Additionally, the nanoparticles had an average size of 21.29 nm, and their superparamagnetic behavior allowed for easy separation after the experiments, as confirmed by the VSM analysis. In addition, the XPS analysis supported the chemical composition of the nano sorbent. The impressive T_2 relaxation activity of the APTES@MNPs was confirmed by a T_2/T_1 relaxation study using low-field MRI. In this study, the loading of daunorubicin was also examined, with the appearance of a pseudo-second-order rate constant (k_2) of 0.00134 mg g^{-1} min^{-1} and an equilibrium adsorption capacity of 16.6 mg g^{-1} at pH ~ 10. A higher percentage of sustained release (72%) was observed at pH ~ 5.2 after 100 h of the desorption experiment, and support for the favorable interaction between the drug and nanoparticles was established by computational results. Such a high percentage of selective pH-driven release of daunorubicin from the dissociation of the drug-nanoparticle complex can provide an effective cancer therapy without affecting healthy cells. Hence, it can be concluded that by using daunorubicin-loaded APTES@MNPs, early detection through MRI with high contrast imaging and simultaneous therapy could be possible in the modern treatment of various deadly cancers. Overall, it could be a potent theranostic agent in the future for the fight against cancer.

Statement of human and animal rights

All experiments were performed without any animals and in accordance with Human and Animal Rights.

Conflicts of interest

The authors declare no conflicts of interest.

Data availability

The supporting data related to this articles is available as supplementary information (SI). The SI file contains figures of daunorubicin adsorption, graph of pseudo first order kinetics, TEM and XPS images, LCMS data, and figure of optimized geometries from computational approach. See DOI: **https://doi.org/10.1039/d5ma00514k**

Acknowledgements

V. Saha would like to thank the University Grants Commission (UGC) for funding the JRF Fellowship Program. (ref no.: 211610176373) and is grateful to the Department of Chemistry, Cooch Behar Panchanan Barma University, for continuous support of the research. We thank Dr. Uday Deshpande (Scientist, UGC-DAE-CSR, Indore, India) and Mr. Sachin Debral (Jr. Engineer, UGC-DAE-CSR, Indore, India) for performing the XPS characterization at their institute. R. Saha thanks the Department of Science & Technology (DST), New Delhi, India, for the DST-INSPIRE Faculty Fellowship (Faculty Registration No. IFA22-CH 378) and C-DAC Patna, Meity, Government of India, for providing the computational facility.

References

1 R. Akter, Md. A. Aziz, A.-R. Al-Betar and A. J. S. Ahammad, Nanomaterials in Agriculture Biosensors, in *ACS Symposium Series*, ed. J. G. Manjunatha, American Chemical Society, Washington, DC, 2025, vol. 1496, pp. 297–313, DOI: **10.1021/bk-2025-1496.ch012**.

2 A. Prasad, R. Kumar, S. Sundaramurthy, A. Suresh, R. Ayub and M. A. Khan, A Review on Assessing Innovative Materials and Technologies for Carbon Dioxide Conversion to Valuables, *Carbon Capture Sci. Technol.*, 2024, **13**, 100287, DOI: **10.1016/j.ccst.2024.100287**.

3 C. Das, N. Nath Ghosh, R. Bhardwaj, K. Narula, P. Mishra and G. Biswas, Enhanced Photocatalytic Degradation of a Hydrocortisone by Biomodified and Biocompatible

Magnetite Nanoparticles and Its Mechanistic Assessment, *J. Ind. Eng. Chem.*, 2023, **128**, 369–382, DOI: **10.1016/j.jiec.2023.08.001**.

4 C. Das, S. Panigrahi, V. Saha, B. Panda, P. Dhak, D. Dhak, V. Pulhani, P. Singhal and G. Biswas, Humic Acid-Nanoceria Composite as a Sustainable Adsorbent for Simultaneous Removal of Uranium(VI), Chromium(VI), and Fluoride Ions from Aqueous Solutions, *Environ. Sci. Pollut. Res.*, 2024, **31**(60), 67429–67441, DOI: **10.1007/s11356-024-32730-2**.

5 M. Yusuf, R. Kumar, M. Ali Khan, M. J. Ahmed, M. Otero, S. Muthu Prabhu, M. Son, J.-H. Hwang, W. Hyoung Lee and B.-H. Jeon, Metal–Organic Framework-Based Composites for Biogas and Natural Gas Uptake: An Overview of Adsorption and Storage Mechanisms of Gaseous Fuels, *Chem. Eng. J.*, 2023, **478**, 147302, DOI: **10.1016/j.cej.2023.147302**.

6 R. Kumar, E. Awino, D. W. Njeri, A. Basu, S. Chattaraj, J. Nayak, S. Roy, G. A. Khan, B. H. Jeon, A. K. Ghosh, S. Pal, S. Banerjee, P. Rout, S. Chakrabortty and S. K. Tripathy, Advancing Pharmaceutical Wastewater Treatment: A Comprehensive Review on Application of Catalytic Membrane Reactor-Based Hybrid Approaches, *J. Water Process Eng.*, 2024, **58**, 104838, DOI: **10.1016/j.jwpe.2024.104838**.

7 R. Tenchov, K. J. Hughes, M. Ganesan, K. A. Iyer, K. Ralhan, L. M. Lotti Diaz, R. E. Bird, J. M. Ivanov and Q. A. Zhou, Transforming Medicine: Cutting-Edge Applications of Nanoscale Materials in Drug Delivery, *ACS Nano*, 2025, **19**(4), 4011–4038, DOI: **10.1021/acsnano.4c09566**.

8 W. J. Stark, P. R. Stoessel, W. Wohlleben and A. Hafner, Industrial Applications of Nanoparticles, *Chem. Soc. Rev.*, 2015, **44**(16), 5793–5805, DOI: **10.1039/C4CS00362D**.

9 Q. A. Pankhurst, J. Connolly, S. K. Jones and J. Dobson, Applications of Magnetic Nanoparticles in Biomedicine, *J. Phys. Appl. Phys.*, 2003, **36**(13), R167–R181, DOI: **10.1088/0022-3727/36/13/201**.

10 C. Jin, K. Wang, A. Oppong-Gyebi and J. Hu, Application of Nanotechnology in Cancer Diagnosis and Therapy – A Mini-Review, *Int. J. Med. Sci.*, 2020, **17**(18), 2964–2973, DOI: **10.7150/ijms.49801**.

11 Y. H. Messinger, P. Gaynon, R. Sposto, J. Van Der Giessen, E. Eckroth, J. Malvar and B. C. Bostrom, Bortezomib Combined with VXLD Chemotherapy Is Highly Effective In Advanced B-Lineage Acute Lymphoblastic Leukemia Allowing Early Study Termination Due to Efficacy. A Therapeutic Advances in Childhood Leukemia (TACL) Consortium Phase II Study, *Blood*, 2011, **118**(21), 251, DOI: **10.1182/blood.V118.21.251.251**.

12 R. Baghban, L. Roshangar, R. Jahanban-Esfahlan, K. Seidi, A. Ebrahimi-Kalan, M. Jaymand, S. Kolahian, T. Javaheri and P. Zare, Tumor Microenvironment Complexity and Therapeutic Implications at a Glance, *Cell Commun. Signaling*, 2020, **18**(1), 59, DOI: **10.1186/s12964-020-0530-4**.

13 J. K. Patra, G. Das, L. F. Fraceto, E. V. R. Campos, M. D. P. Rodriguez-Torres, L. S. Acosta-Torres, L. A. Diaz-Torres, R. Grillo, M. K. Swamy, S. Sharma, S. Habtemariam and H.-S. Shin, Nano Based Drug Delivery Systems: Recent Developments and Future Prospects, *J. Nanobiotechnol.*, 2018, **16**(1), 71, DOI: **10.1186/s12951-018-0392-8**.

14 S. Mukherjee, L. Liang and O. Veiseh, Recent Advancements of Magnetic Nanomaterials in Cancer Therapy, *Pharmaceutics*, 2020, **12**(2), 147, DOI: **10.3390/pharmaceutics12020147**.

15 B. Chen, J. Wang, B. Chen, J. Cheng, X. G. Cai, P. Chen, Z. Yu and X. Wang, Synthesis and Antitumor Efficacy of Daunorubicin-Loaded Magnetic Nanoparticles, *Int. J. Nanomed.*, 2011, 203, DOI: **10.2147/IJN.S16165**.

16 O. Veiseh, C. Sun, J. Gunn, N. Kohler, P. Gabikian, D. Lee, N. Bhattarai, R. Ellenbogen, R. Sze, A. Hallahan, J. Olson and M. Zhang, Optical and MRI Multifunctional Nanoprobe for Targeting Gliomas, *Nano Lett.*, 2005, **5**(6), 1003–1008, DOI: **10.1021/nl0502569**.

17 P. Kesharwani, K. Jain and N. K. Jain, Dendrimer as Nanocarrier for Drug Delivery, *Prog. Polym. Sci.*, 2014, **39**(2), 268–307, DOI: **10.1016/j.progpolymsci.2013.07.005**.

18 H. Peng, C. Wang, X. Xu, C. Yu and Q. Wang, An Intestinal Trojan Horse for Gene Delivery, *Nanoscale*, 2015, **7**(10), 4354–4360, DOI: **10.1039/C4NR06377E**.

19 F. Barahuie, D. Dorniani, S. Bullo, S. Gothai, M. Z. Hussein, A. K. Pandurangan, P. Arulselvan and M. E. Norhaizan, Sustained Release of Anticancer Agent Phytic Acid from Its Chitosan-Coated Magnetic Nanoparticles for Drug-Delivery System, *Int. J. Nanomed.*, 2017, **12**, 2361–2372, DOI: **10.2147/IJN.S126245**.

20 Y. Zhao, Z. Qiu and J. Huang, Preparation and Analysis of Fe_3O_4 Magnetic Nanoparticles Used as Targeted-Drug Carriers, *Chin. J. Chem. Eng.*, 2008, **16**(3), 451–455, DOI: **10.1016/S1004-9541(08)60104-4**.

21 S. Kayal and R. V. Ramanujan, Doxorubicin Loaded PVA Coated Iron Oxide Nanoparticles for Targeted Drug Delivery, *Mater. Sci. Eng., C*, 2010, **30**(3), 484–490, DOI: **10.1016/j.msec.2010.01.006**.

22 T. Neuberger, B. Schöpf, H. Hofmann, M. Hofmann and B. Von Rechenberg, Superparamagnetic Nanoparticles for Biomedical Applications: Possibilities and Limitations of a New Drug Delivery System, *J. Magn. Magn. Mater.*, 2005, **293**(1), 483–496, DOI: **10.1016/j.jmmm.2005.01.064**.

23 V. C. Karade, A. Sharma, R. P. Dhavale, R. P. Dhavale, S. R. Shingte, P. S. Patil, J. H. Kim, D. R. T. Zahn, A. D. Chougale, G. Salvan and P. B. Patil, APTES Monolayer Coverage on Self-Assembled Magnetic Nanospheres for Controlled Release of Anticancer Drug Nintedanib, *Sci. Rep.*, 2021, **11**(1), 5674, DOI: **10.1038/s41598-021-84770-0**.

24 M. Norouzi, V. Yathindranath, J. A. Thliveris, B. M. Kopec, T. J. Siahaan and D. W. Miller, Doxorubicin-Loaded Iron Oxide Nanoparticles for Glioblastoma Therapy: A Combinational Approach for Enhanced Delivery of Nanoparticles, *Sci. Rep.*, 2020, **10**(1), 11292, DOI: **10.1038/s41598-020-68017-y**.

25 M. Luo, L. Zhou, Z. Huang, B. Li, E. C. Nice, J. Xu and C. Huang, Antioxidant Therapy in Cancer: Rationale and Progress, *Antioxidants*, 2022, **11**(6), 1128, DOI: **10.3390/antiox11061128**.

26 W. Hong, C.-C. Liu, H. Zhang, Z. Chen, M. Xiao and L. Xu, Cancer Cell Preferential Penetration and pH-Responsive

Drug Delivery of Oligorutin, *Biomacromolecules*, 2021, **22**(9), 3679–3691, DOI: **10.1021/acs.biomac.1c00268**.

27 Z. Gong, H. Zhao and J. Bai, pH-Responsive Drug-Loaded Peptides Enhance Drug Accumulation and Promote Apoptosis in Tumor Cells, *Colloids Surf., B*, 2024, **239**, 113954, DOI: **10.1016/j.colsurfb.2024.113954**.

28 R. Thirumaran, G. C. Prendergast and P. B. Gilman, Cytotoxic Chemotherapy in Clinical Treatment of Cancer, *Cancer Immunotherapy*, Elsevier, 2007, pp. 101–116, DOI: **10.1016/B978-012372551-6/50071-7**.

29 B. Zhang, Y. Wang, J. Zhang, S. Qiao, Z. Fan, J. Wan and K. Chen, Well-Defined 3-Aminopropyltriethoxysilane Functionalized Magnetite Nanoparticles and Their Adsorption Performance for Partially Hydrolyzed Polyacrylamide from Aqueous Solution, *Colloids Surf., A*, 2020, **586**, 124288, DOI: **10.1016/j.colsurfa.2019.124288**.

30 V. R. Khabibullin, M. R. Chetyrkina, S. I. Obydennyy, S. V. Maksimov, G. V. Stepanov and S. N. Shtykov, Study on Doxorubicin Loading on Differently Functionalized Iron Oxide Nanoparticles: Implications for Controlled Drug-Delivery Application, *Int. J. Mol. Sci.*, 2023, **24**(5), 4480, DOI: **10.3390/ijms24054480**.

31 A. Avasthi, C. Caro, E. Pozo-Torres, M. P. Leal and M. L. García-Martín, Magnetic Nanoparticles as MRI Contrast Agents, *Top. Curr. Chem.*, 2020, **378**(3), 40, DOI: **10.1007/s41061-020-00302-w**.

32 J. Ge, Y. Zhang, Z. Dong, J. Jia, J. Zhu, X. Miao and B. Yan, Initiation of Targeted Nanodrug Delivery in Vivo by a Multifunctional Magnetic Implant, *ACS Appl. Mater. Interfaces*, 2017, **9**(24), 20771–20778, DOI: **10.1021/acsami.7b05009**.

33 J. You, L. Wang, Y. Zhao and W. Bao, A Review of Amino-Functionalized Magnetic Nanoparticles for Water Treatment: Features and Prospects, *J. Cleaner Prod.*, 2021, **281**, 124668, DOI: **10.1016/j.jclepro.2020.124668**.

34 C. Das, S. Sen, T. Singh, T. Ghosh, S. S. Paul, T. W. Kim, S. Jeon, D. K. Maiti, J. Im and G. Biswas, Green Synthesis, Characterization and Application of Natural Product Coated Magnetite Nanoparticles for Wastewater Treatment, *Nanomaterials*, 2020, **10**(8), 1615, DOI: **10.3390/nano10081615**.

35 C. Das, N. N. Ghosh, V. Pulhani, G. Biswas and P. Singhal, Bio-Functionalized Magnetic Nanoparticles for Cost-Effective Adsorption of U(VI): Experimental and Theoretical Investigation, *RSC Adv.*, 2023, **13**(22), 15015–15023, DOI: **10.1039/D3RA00799E**.

36 A. El Hachmi, S. Sen, R. Mondal, M. Paul, A. Saha, J. Im and G. Biswas, Structural, Morphological, Magnetic and Optical Properties of Jeanbandyite Prepared by the Co-Precipitation Method, *Mater. Today Commun.*, 2023, **34**, 105358, DOI: **10.1016/j.mtcomm.2023.105358**.

37 B. Saif, C. Wang, D. Chuan and S. Shuang, Synthesis and Characterization of Fe_3O_4 Coated on APTES as Carriers for Morin-Anticancer Drug, *J. Biomater. Nanobiotechnol.*, 2015, **06**(04), 267–275, DOI: **10.4236/jbnb.2015.64025**.

38 F. Hosseini, M. Sadjadi and N. Farhadyar, Fe_3O_4 Nanoparticles Modified with APTES as the Carrier for (+)-(*S*)-2-(6-Methoxynaphthalen-2-Yl) Propanoic Acid (Naproxen) and (RS) 2-(3-Benzoylphenyl)-Propionic Acid (Ketoprofen) Drug, *Orient. J. Chem.*, 2014, **30**(4), 1609–1618, DOI: **10.13005/ojc/300420**.

39 M. Aravind, M. Amalanathan and M. S. M. Mary, Synthesis of TiO_2 Nanoparticles by Chemical and Green Synthesis Methods and Their Multifaceted Properties, *SN Appl. Sci.*, 2021, **3**(4), 409, DOI: **10.1007/s42452-021-04281-5**.

40 M. Alimohammadian, S. Azizian and B. Sohrabi, Preparation of the Graphene-Based Smart Hydrophobic Nanocomposite and Its Application in Oil/Water Separation, *Sci. Rep.*, 2023, **13**(1), 19816, DOI: **10.1038/s41598-023-46520-2**.

41 S. Mourdikoudis, R. M. Pallares and N. T. K. Thanh, Characterization Techniques for Nanoparticles: Comparison and Complementarity upon Studying Nanoparticle Properties, *Nanoscale*, 2018, **10**(27), 12871–12934, DOI: **10.1039/C8NR02278J**.

42 S. Chandra, S. Mehta, S. Nigam and D. Bahadur, Dendritic Magnetite Nanocarriers for Drug Delivery Applications, *New J. Chem.*, 2010, **34**(4), 648, DOI: **10.1039/b9nj00609e**.

43 A. Sebastian, A. Nangia and M. N. V. Prasad, Cadmium and Sodium Adsorption Properties of Magnetite Nanoparticles Synthesized from Hevea Brasiliensis Muell. Arg. Bark: Relevance in Amelioration of Metal Stress in Rice, *J. Hazard. Mater.*, 2019, **371**, 261–272, DOI: **10.1016/j.jhazmat.2019.03.021**.

44 H. Jahangirian, E. Ghasemian Lemraski, T. J. Webster, R. Rafiee-Moghaddam and Y. Abdollahi, A Review of Drug Delivery Systems Based on Nanotechnology and Green Chemistry: Green Nanomedicine, *Int. J. Nanomed.*, 2017, **12**, 2957–2978, DOI: **10.2147/IJN.S127683**.

45 M. A. Obeid, M. M. Al Qaraghuli, M. Alsaadi, A. R. Alzahrani, K. Niwasabutra and V. A. Ferro, Delivering Natural Products and Biotherapeutics to Improve Drug Efficacy, *Ther. Delivery*, 2017, **8**(11), 947–956, DOI: **10.4155/tde-2017-0060**.

46 S. Joshi, V. K. Garg, N. Kataria and K. Kadirvelu, Applications of Fe_3O_4@AC Nanoparticles for Dye Removal from Simulated Wastewater, *Chemosphere*, 2019, **236**, 124280, DOI: **10.1016/j.chemosphere.2019.07.011**.

47 M. Sharifi, S. M. Rezayat, K. Akhtari, A. Hasan and M. Falahati, Fabrication and Evaluation of Anti-Cancer Efficacy of Lactoferrin-Coated Maghemite and Magnetite Nanoparticles, *J. Biomol. Struct. Dyn.*, 2020, **38**(10), 2945–2954, DOI: **10.1080/07391102.2019.1650114**.

48 C. Rajeevgandhi, S. Bharanidharan, S. Savithiri, L. Guganathan, P. Sugumar, K. Sathiyamurthy and K. Mohan, Synthesis, Characterizations and Quantum Chemical Calculations of the Spinel Structure of Fe_3O_4 Nanoparticles, *J. Mater. Sci.: Mater. Electron.*, 2020, **31**(23), 21419–21430, DOI: **10.1007/s10854-020-04656-1**.

49 J. Jayabharathi, A. Prabhakaran, C. Karunakaran, V. Thanikachalam and M. Sundharesan, Structural, Optical and Photoconductivity Characteristics of Pristine $FeO{\cdot}Fe_2O_3$ and NTPI–$FeO{\cdot}Fe_2O_3$ Nanocomposite: Aggregation Induced Emission Enhancement of Fluorescent Organic Nanoprobe of Thiophene Appended Phenanthrimidazole Derivative, *RSC Adv.*, 2016, **6**(22), 18718–18736, DOI: **10.1039/c5ra25545g**.

50 S. Wang, J. Li, L. Chen, J. Zeng and M. Gao, Fe^{2+}-Dominated Relaxometric Properties of Iron Oxide Nanoparticles as MRI

Contrast Agents, *J. Phys. Chem. Lett.*, 2024, 8861–8866, DOI: 10.1021/acs.jpclett.4c01876.

51 N. Lee and T. Hyeon, Designed Synthesis of Uniformly Sized Iron Oxide Nanoparticles for Efficient Magnetic Resonance Imaging Contrast Agents, *Chem. Soc. Rev.*, 2012, **41**(7), 2575–2589, DOI: 10.1039/C1CS15248C.

52 K.-Y. Yang, L.-C. Lin, T.-Y. Tseng, S.-C. Wang and T.-H. Tsai, Oral Bioavailability of Curcumin in Rat and the Herbal Analysis from Curcuma Longa by LC–MS/MS, *J. Chromatogr. B: Anal. Technol. Biomed. Life Sci.*, 2007, **853**(1–2), 183–189, DOI: 10.1016/j.jchromb.2007.03.010.

53 F. Ahmadpoor, A. Masood, N. Feliu, W. J. Parak and S. A. Shojaosadati, The Effect of Surface Coating of Iron Oxide Nanoparticles on Magnetic Resonance Imaging Relaxivity, *Front. Nanotechnol.*, 2021, **3**, 644734, DOI: 10.3389/fnano.2021.644734.

54 M.-A. Karageorgou, S. Vranješ-Djurić, M. Radović, A. Lyberopoulou, B. Antić, M. Rouchota, M. Gazouli, G. Loudos, S. Xanthopoulos, Z. Sideratou, D. Stamopoulos, P. Bouziotis and C. Tsoukalas, Gallium-68 Labeled Iron Oxide Nanoparticles Coated with 2,3-Dicarboxypropane-1,1-Diphosphonic Acid as a Potential PET/MR Imaging Agent: A Proof-of-Concept Study, *Contrast Media Mol. Imaging*, 2017, **2017**, 1–13, DOI: 10.1155/2017/6951240.

55 V. A. Zeitler and C. A. Brown, The Infrared Spectra of Some Ti–O–Si, Ti–O–Ti and Si–O–Si Compounds, *J. Phys. Chem.*, 1957, **61**(9), 1174–1177, DOI: 10.1021/j150555a010.

56 Y. P. Yew, K. Shameli, M. Miyake, N. Kuwano, N. B. Bt Ahmad Khairudin, S. E. Bt Mohamad and K. X. Lee, Green Synthesis of Magnetite (Fe_3O_4) Nanoparticles Using Seaweed (Kappaphycus Alvarezii) Extract, *Nanoscale Res. Lett.*, 2016, **11**(1), 276, DOI: 10.1186/s11671-016-1498-2.

57 D. Ranmadugala, A. Ebrahiminezhad, M. Manley-Harris, Y. Ghasemi and A. Berenjian, Impact of 3-Aminopropyltriethoxysilane-Coated Iron Oxide Nanoparticles on Menaquinone-7 Production Using B. Subtilis, *Nanomaterials*, 2017, **7**(11), 350, DOI: 10.3390/nano7110350.

58 H. Khanjanzadeh, R. Behrooz, N. Bahramifar, W. Gindl-Altmutter, M. Bacher, M. Edler and T. Griesser, Surface Chemical Functionalization of Cellulose Nanocrystals by 3-Aminopropyltriethoxysilane, *Int. J. Biol. Macromol.*, 2018, **106**, 1288–1296, DOI: 10.1016/j.ijbiomac.2017.08.136.

59 M. Kristl, U. Ostroško, I. Ban, I. Petrinić and J. Stergar, Thermal Study of APTES-Functionalized Magnetite Nanoparticles with Citric Acid and Polyacrylic Acid for Advanced Forward Osmosis Systems, *J. Therm. Anal. Calorim.*, 2024, **149**(19), 10449–10463, DOI: 10.1007/s10973-024-12983-2.

60 S. Chandra, S. Mehta, S. Nigam and D. Bahadur, Dendritic Magnetite Nanocarriers for Drug Delivery Applications, *New J. Chem.*, 2010, **34**(4), 648, DOI: 10.1039/b9nj00609e.

61 P. R. Ghutepatil, A. B. Salunkhe, V. M. Khot and S. H. Pawar, APTES (3-Aminopropyltriethoxy Silane) Functionalized $MnFe_2O_4$ Nanoparticles: A Potential Material for Magnetic Fluid Hyperthermia, *Chem. Pap.*, 2019, **73**(9), 2189–2197, DOI: 10.1007/s11696-019-00768-z.

62 P. Cheera, S. Karlapudi, G. Sellola and V. Ponneri, A Facile Green Synthesis of Spherical Fe_3O_4 Magnetic Nanoparticles and Their Effect on Degradation of Methylene Blue in Aqueous Solution, *J. Mol. Liq.*, 2016, **221**, 993–998, DOI: 10.1016/j.molliq.2016.06.006.

63 M. Filippousi, M. Angelakeris, M. Katsikini, E. Paloura, I. Efthimiopoulos, Y. Wang, D. Zamboulis and G. Van Tendeloo, Surfactant Effects on the Structural and Magnetic Properties of Iron Oxide Nanoparticles, *J. Phys. Chem. C*, 2014, **118**(29), 16209–16217, DOI: 10.1021/jp5037266.

64 S. J. Kemp, R. M. Ferguson, A. P. Khandhar and K. M. Krishnan, Monodisperse Magnetite Nanoparticles with Nearly Ideal Saturation Magnetization, *RSC Adv.*, 2016, **6**(81), 77452–77464, DOI: 10.1039/C6RA12072E.

65 S.-M. Taghizadeh, M. B. Ghoshoon, A. Berenjian, Y. Ghasemi, A. Dehshahri and A. Ebrahiminezhad, Impacts of Magnetic Immobilization on the Recombinant Proteins Structure Produced in Pichia Pastoris System, *Mol. Biotechnol.*, 2021, **63**(1), 80–89, DOI: 10.1007/s12033-020-00286-4.

66 A. Medina, F. A. Casado-Carmona, Á. I. López-Lorente and S. Cárdenas, Magnetic Graphene Oxide Composite for the Microextraction and Determination of Benzophenones in Water Samples, *Nanomaterials*, 2020, **10**(1), 168, DOI: 10.3390/nano10010168.

67 M. Behera, N. Kumari, K. Raza and R. Singh, Fabrication of Glutathione Functionalized Self-Assembled Magnetite Nanochains for Effective Removal of Crystal Violet and Phenol Red Dye from Aqueous Matrix, *Environ. Sci. Pollut. Res.*, 2022, **29**(48), 72260–72278, DOI: 10.1007/s11356-022-19520-4.

68 L. Slavov, M. V. Abrashev, T. Merodiiska, Ch Gelev, R. E. Vandenberghe, I. Markova-Deneva and I. Nedkov, Raman Spectroscopy Investigation of Magnetite Nanoparticles in Ferrofluids, *J. Magn. Magn. Mater.*, 2010, **322**(14), 1904–1911, DOI: 10.1016/j.jmmm.2010.01.005.

69 Y. Sato, R. Hayami and T. Gunji, Characterization of NMR, IR, and Raman Spectra for Siloxanes and Silsesquioxanes: A Mini Review, *J. Sol-Gel Sci. Technol.*, 2022, **104**(1), 36–52, DOI: 10.1007/s10971-022-05920-y.

70 T. Yamashita and P. Hayes, Analysis of XPS Spectra of Fe^{2+} and Fe^{3+} Ions in Oxide Materials, *Appl. Surf. Sci.*, 2008, **254**(8), 2441–2449, DOI: 10.1016/j.apsusc.2007.09.063.

71 M. C. Biesinger, B. P. Payne, A. P. Grosvenor, L. W. M. Lau, A. R. Gerson and R. St. C. Smart, Resolving Surface Chemical States in XPS Analysis of First Row Transition Metals, Oxides and Hydroxides: Cr, Mn, Fe, Co and Ni, *Appl. Surf. Sci.*, 2011, **257**(7), 2717–2730, DOI: 10.1016/j.apsusc.2010.10.051.

72 G. P. Lopinski, O. Kodra, F. Kunc, D. C. Kennedy, M. Couillard and L. J. Johnston, X-Ray Photoelectron Spectroscopy of Metal Oxide Nanoparticles: Chemical Composition, Oxidation State and Functional Group Content, *Nanoscale Adv.*, 2025, **7**(6), 1671–1685, DOI: 10.1039/D4NA00943F.

73 W. A. Talavera-Pech, A. Esparza-Ruiz, P. Quintana-Owen, A. R. Vilchis-Nestor, C. Carrera-Figueiras and A. Ávila-Ortega, Effects

of Different Amounts of APTES on Physicochemical and Structural Properties of Amino-Functionalized MCM-41-MSNs, *J. Sol-Gel Sci. Technol.*, 2016, **80**(3), 697–708, DOI: **10.1007/s10971-016-4163-4**.

74 E. Tanasa, C. Zaharia, I.-C. Radu, V.-A. Surdu, B. S. Vasile, C.-M. Damian and E. Andronescu, Novel Nanocomposites Based on Functionalized Magnetic Nanoparticles and Polyacrylamide: Preparation and Complex Characterization, *Nanomaterials*, 2019, **9**(10), 1384, DOI: **10.3390/nano9101384**.

75 C. Das, S. Singh, S. Bhakta, P. Mishra and G. Biswas, Bio-Modified Magnetic Nanoparticles with Terminalia Arjuna Bark Extract for the Removal of Methylene Blue and Lead(II) from Simulated Wastewater, *Chemosphere*, 2022, **291**, 132673, DOI: **10.1016/j.chemosphere.2021.132673**.

76 R. Qiao, C. Yang and M. Gao, Superparamagnetic Iron Oxide Nanoparticles: From Preparations to in Vivo MRI Applications, *J. Mater. Chem.*, 2009, **19**(35), 6274, DOI: **10.1039/b902394a**.

77 M. Z. Iqbal, X. Ma, T. Chen, L. Zhang, W. Ren, L. Xiang and A. Wu, Silica-Coated Super-Paramagnetic Iron Oxide Nanoparticles (SPIONPs): A New Type Contrast Agent of T_1 Magnetic Resonance Imaging (MRI), *J. Mater. Chem. B*, 2015, **3**(26), 5172–5181, DOI: **10.1039/C5TB00300H**.

78 H. Jung, B. Park, C. Lee, J. Cho, J. Suh, J. Park, Y. Kim, J. Kim, G. Cho and H. Cho, Dual MRI T_1 and T_2(*) Contrast with Size-Controlled Iron Oxide Nanoparticles, *Nanomedicine*, 2014, **10**(8), 1679–1689, DOI: **10.1016/j.nano.2014.05.003**.

79 U. I. Tromsdorf, O. T. Bruns, S. C. Salmen, U. Beisiegel and H. Weller, A Highly Effective, Nontoxic T_1 MR Contrast Agent Based on Ultrasmall PEGylated Iron Oxide Nanoparticles, *Nano Lett.*, 2009, **9**(12), 4434–4440, DOI: **10.1021/nl902715v**.

80 L. Zeng, W. Ren, J. Zheng, P. Cui and A. Wu, Ultrasmall Water-Soluble Metal-Iron Oxide Nanoparticles as T_1-Weighted Contrast Agents for Magnetic Resonance Imaging, *Phys. Chem. Chem. Phys.*, 2012, **14**(8), 2631, DOI: **10.1039/c2cp23196d**.

81 Y. Gossuin, E. Martin, Q. L. Vuong, J. Delroisse, S. Laurent, D. Stanicki and C. Rousseau, Characterization of Commercial Iron Oxide Clusters with High Transverse Relaxivity, *J. Magn. Reson. Open*, 2022, **10–11**, 100054, DOI: **10.1016/j.jmro.2022.100054**.

82 H. Zhou, J. Tang, J. Li, W. Li, Y. Liu and C. Chen, In Vivo Aggregation-Induced Transition between T_1 and T_2 Relaxations of Magnetic Ultra-Small Iron Oxide Nanoparticles in Tumor Microenvironment, *Nanoscale*, 2017, **9**(9), 3040–3050, DOI: **10.1039/C7NR00089H**.